New approaches for imaging tumour responses to treatment

Kevin Brindle

Abstract | Tumour responses to treatment are still largely assessed from imaging measurements of reductions in tumour size. However, this can take several weeks to become manifest and in some cases may not occur at all, despite a positive response to treatment. There has been considerable interest, therefore, in non-invasive techniques for imaging tissue function that can give early evidence of response. These can be used in clinical trials of new drugs to give an early indication of drug efficacy, and subsequently in the clinic to select the most effective therapy at an early stage of treatment.

A better understanding of the molecular signature of cancer has allowed the development of a new generation of anticancer drugs that target specific molecular entities, such as receptors, genes or signalling pathways. However, DNA microarray-based disease profiling, together with the results of clinical trials using targeted therapies, have clearly demonstrated the intrinsic heterogeneity of human tumours, both genetically and phenotypically[1,2]. Patients with similar tumour types frequently have markedly different responses to the same therapy. The development of these novel targeted therapies could benefit significantly, therefore, from the introduction of imaging methods that allow an early assessment of treatment response in individual patients. These could be used in early-stage clinical trials to provide a rapid indication of drug efficacy. For example, dynamic contrast agent-enhanced magnetic resonance imaging (DCE-MRI) measurements of tumour perfusion were used in a phase I trial of the anti-vascular drug combretastatin A4 3-*O*-phosphate[3]. Subsequently these imaging techniques could be used in the clinic, where they would allow the clinician to rapidly assess the effectiveness of a new therapy in individual patients. Ineffective treatments could be abandoned at an early stage and more effective treatments selected, with attendant welfare benefits for the patient and cost benefits for the health-care system.

Tumour responses to treatment have conventionally been assessed from measurements of tumour size[4], using morphological imaging techniques such as X-ray computed tomography (CT) and MRI. The limitations of this approach for predicting clinical benefit have been discussed[5]. In recent years, these measurements have been supplemented by imaging of tissue function, which has often been termed molecular imaging and is defined by a pioneer of this field as the "*in vivo* characterization and measurement of biologic processes at the cellular and molecular level."[6] The aim is to transfer into a conventional image of tissue morphology, often using specific probe molecules, information about the underlying cell biology, physiology and biochemistry. Such information could show whether a drug has reached its target, whether the function of that target has been modulated and whether this has led to changes in tumour biology, long before there is any evidence of changes in tumour size. This Review will briefly outline the basic principles of the different imaging modalities, discuss how these imaging techniques have been used for response monitoring in preclinical and clinical studies, discuss new developments in imaging and speculate where this field might go in the future.

Department of Biochemistry, University of Cambridge, 80 Tennis Court Road, Cambridge, CB2 1GA, UK, and Cancer Research UK Cambridge Research Institute, Li Ka Shing Centre, Robinson Way, Cambridge, CB2 0RE, UK.
e-mail: kmb@mole.bio.cam.ac.uk
doi:10.1038/nrc2289
Published online
18 January 2008

Imaging modalities

Developments in molecular imaging have been driven by the availability of clinical imaging modalities, such as X-ray CT, positron-emission tomography (PET), single photon-emission computed tomography (SPECT), MRI and ultrasound, in relatively high-resolution configurations that can be used in the laboratory to image small animals, particularly mice. In addition to clinically used imaging modalities, optical (bioluminescence and fluorescence) imaging has been a key technique for molecular imaging[7].

X-ray CT. CT images are obtained by rotating a low-energy X-ray source and detector around the subject to acquire a series of projections. These are then used to construct a three-dimensional image. Contrast in the image arises because of differential tissue absorption of X-rays, although the contrast is not as strong as that obtained with MRI. Image resolutions of 100 μm are

At a glance

- Detection of the early responses of tumours to treatment could be used to guide subsequent therapy, allowing rapid selection of the most appropriate therapy, with attendant welfare benefits for the patient and cost benefits for the health-care system.
- Tumour responses to treatment are conventionally assessed by imaging measurements of tumour size. However, tumour shrinkage can take weeks or even months to become apparent or, with some therapies, might not occur at all, despite a positive response to treatment.
- Imaging measurements of tumour biochemistry or cell biology can give an earlier indication of whether a tumour is responding to treatment than measurements of tumour size. For example, measurements of the reduction in tumour uptake of a radiolabelled glucose analogue, 2-[^{18}F]fluoro-2-deoxy-D-glucose, are already used clinically to detect tumour responses to treatment, often before there is any change in tumour size.
- The radionuclide imaging techniques, positron-emission tomography and single photon-emission computed tomography, can be used to monitor receptor expression using appropriately labelled receptor ligands. As these techniques are so sensitive (they can detect concentrations in the 10^{-12}–10^{-10} M range), the agents can be administered at sub-pharmacological doses.
- Labelling of cell metabolites (for example, amino acids, acetate, the glucose analogue fluorodeoxyglucose) with positron-emitting isotopes (^{11}C and ^{18}F) allows imaging of tumour metabolism in the clinic.
- Magnetic resonance imaging of the protons in tissue water gives relatively high-resolution images of tissue morphology. By using receptor ligands that have been labelled with paramagnetic tags that affect the spin relaxation times, magnetic resonance imaging measurements of tissue water can be used to image receptor expression indirectly.
- Magnetic resonance spectroscopy (MRS) can be used to detect tumour metabolites *in vivo*. Phosphorus-31 MRS can be used to monitor the levels of ATP, inorganic phosphate and intracellular pH and ^{1}H MRS the levels of various abundant metabolites, including lactate, neutral lipids and phospholipid metabolites, such as phosphocholine.
- Nuclear spin hyperpolarization can be used to dramatically enhance the sensitivity (> 10,000×) of the magnetic resonance experiment. Hyperpolarization of injected molecules allows spectroscopic imaging of their distribution in the body and subsequent metabolism.
- The availability of these clinical imaging modalities in configurations that can be used with animal models of disease in the laboratory should promote the translation of new imaging techniques from the laboratory into the clinic.

obtainable in animal studies in ~15 min of data acquisition. Higher-resolution images (50 μm) are possible with longer scan times; however, radiation dose can limit repeat imaging of the same animal. At relatively high resolution (for example, 50 × 50 × 50 μm), doses range from 100 to 300 mGy, or about 10× more than a typical human CT examination[8]. CT is often used to provide images of tissue anatomy and is increasingly being used in conjunction with PET, where it provides an anatomical context to the relatively low-resolution PET image. In the clinic the fusion of X-ray CT and PET images has led to improvements in tumour detection[9].

Ultrasound. The relatively low cost, ease of use, sensitivity and speed of imaging make this an attractive imaging modality in the laboratory, particularly when looking for early signs of tumour formation in mouse models. A system designed specifically for mouse imaging is available commercially and this system also includes Doppler measurements of blood flow velocity. These can be used, for example, to monitor tumour vascular disruption in real time following anti-vascular therapy[10] (FIG. 1). Ultrasound imaging has also been shown to be capable of detecting tumour-cell apoptosis, or programmed cell death, *in vivo* following the administration of chemotherapy in an animal model[11]. Tissue stiffness can be imaged by detecting the effects of small, local tissue deformations (elastography) and has been used to enhance the sensitivity of detection of malignant lesions in the breast, which can show large changes in elasticity compared with surrounding normal tissue[12]. Similar measurements have been made using MRI[13]. As there may be changes in tissue architecture following therapy, it seems plausible that elastography might also be used to detect treatment response. Molecular imaging with ultrasound has involved the use of targeted microbubbles, which produce an acoustic signal because of their resonant properties in the ultrasound field. Tumour targeting is achieved by chemical modification of the microbubble shell or by attaching a targeting ligand. For example, tumour-induced angiogenesis has been detected using microbubbles targeted at the integrin $\alpha_v\beta_3$, which is upregulated on proliferating endothelial cells. Targeting was achieved by conjugation with a peptide containing the Arg–Gly–Asp (RGD) motif, which binds to the integrin[14]. However, the relatively large size of the microbubbles (1–4 μm) means that they cannot leave the intravascular space and molecular imaging is limited to this compartment.

MRI. This technique was developed in the early 1970s and led to the award of the Nobel Prize for Physiology and Medicine to Paul Lauterbur and Peter Mansfield in 2003. MRI involves the detection of nuclear spin reorientation in an applied magnetic field (FIG. 2). Because the interaction is so weak the technique is insensitive and imaging is usually restricted to detection of water protons (FIG. 3), as water is abundant in tissue and the proton is second only to tritium in sensitivity to MR detection. Image resolution is limited by the sensitivity of signal detection and, at the relatively low magnetic field strengths used in the clinic (1.5–3 T), is in the range of 2–3 mm. At the higher field strengths commonly in use in the laboratory (7–9.4 T), where sensitivity is higher, the resolution is typically 50–100 μm, although in fixed tissues isotropic image resolutions of 10 μm are possible[15]. The time taken to acquire the image depends, in part, on the resolution required and is typically several minutes, although fast imaging techniques allow cine-imaging in which single images are acquired in tens of milliseconds.

MRI of tissue water protons is often used, like CT, to provide images of anatomy. However, as there are many different mechanisms for generating contrast in the MR image, it is better suited than CT to molecular imaging of tissue function. By attaching paramagnetic labels to appropriate targeting ligands (BOX 1), ^{1}H MRI of tissue water protons can be used to indirectly image membrane receptors, such as ERBB2 (also known as HER-2) on breast cancer cells[16], the integrin $\alpha_v\beta_3$ on angiogenic endothelial cells[17,18] and the phospholipid

Isotropic image resolutions
Image resolution in the three orthogonal image axes.

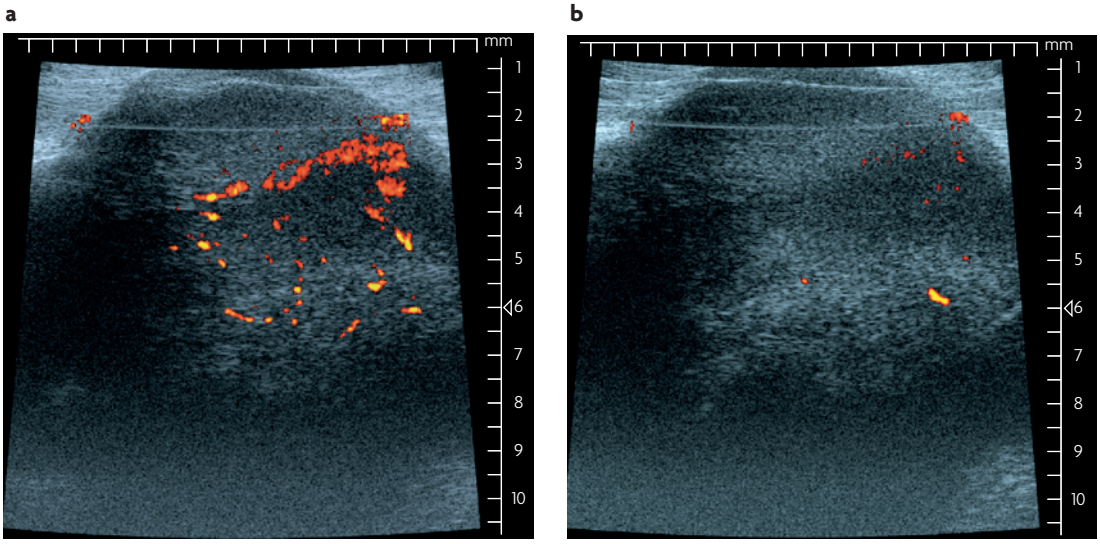

Figure 1 | **Ultrasound imaging.** Ultrasound images are obtained when high-frequency sound waves emitted from a transducer placed on the subject are reflected back from underlying tissue structures. Clinical ultrasound instrumentation operates at frequencies of between 7.5 and 15 MHz, with a spatial resolution of 300–500 μm. At higher frequencies (40–50 MHz) the resolution is 50–100 μm, making it suitable for relatively high-resolution imaging in small animals, although at these frequencies ultrasound penetration is limited to 5–10 mm in soft tissues. The images show power Doppler ultrasound measurements from a subcutaneous murine lymphoma before (**a**) and 15 min after (**b**) administration of the anti-vascular agent combretastatin A4 3-*O*-phosphate at a concentration of 100 mg kg body weight^{-1}. Regions of blood flow are depicted in colour. Data courtesy of D. Hu, Department of Biochemistry, Cambridge University, Cambridge, UK.

phosphatidylserine on the surface of apoptotic cells[19–21]. However, as these receptors are usually present at low concentrations, it is frequently necessary to use high concentrations of the paramagnetic label, for example, liposomes loaded with multiple Gd^{3+} chelates[17]. Cells can also be labelled with paramagnetic labels and tracked non-invasively *in vivo* at relatively high resolution (reviewed in REFS 22,23). Although MR image resolution *in vivo* is not at the level where single cells can be observed it is, nevertheless, possible to image the presence of single cells using iron oxide-based nanometre- or micrometre-sized particles, as the effect of the particle on the surrounding magnetic field extends way beyond the boundaries of the cell[24]. The technique has been used, for example, to track implanted stem cells in the brain and spinal cord[25,26], to monitor T-cell trafficking in immunogenic tumours[27,28] and to image the location of implanted dendritic cells in the clinic[29]. Cells have also been labelled with a perfluoropolyether and the cells tracked using ^{19}F MRI[30].

Different NMR-active nuclei resonate at different frequencies (so, at 9.4 T, ^{1}H resonates at 400 MHz, ^{31}P at 161 MHz and ^{13}C at 100 MHz). However, for any nucleus, these resonance frequencies vary (on the order of a few kilohertz, depending on the nucleus) according to their electronic environment: the protons in a water molecule resonate at a different frequency to the protons in the methyl group of lactate. This is known as chemical shift and is the reason that magnetic resonance spectroscopy (MRS) has been such a powerful technique in analytical chemistry and protein structure determination. These spectroscopic measurements can also be made *in vivo*, in systems ranging from isolated cells to the human brain, in which they can be used to monitor tissue biochemistry (FIG. 4). As the patterns of metabolites are characteristic of a particular tumour type it is hoped that measurements such as those shown in FIG. 4 could eventually be used to diagnose and grade brain tumours non-invasively and thus remove the necessity for tumour biopsy, with its associated morbidity[31,32]. Phosphorus-31 MRS can be used to monitor bioenergetic status by measuring the levels of ATP, inorganic phosphate and phosphocreatine in tissues such as brain and muscle, and phospholipid metabolism, particularly in tumours, from measurements of the levels of phospholipid metabolites, such as phosphocholine[33]. In conjunction with ^{13}C-labelled molecules, ^{13}C MRS can be used to follow metabolic interconversions[34] (note that the naturally abundant isotope of carbon, ^{12}C, is not NMR-active). As the ^{31}P and ^{13}C nuclei are much less sensitive to detection than ^{1}H, and cellular metabolites are present at much lower concentrations than tissue water (in the millimolar range versus ~40 M for water protons in tissue), image resolution is much lower, with voxel volumes in the millilitre range. However, the dynamic nuclear polarization technique described in BOX 2 and FIG. 5, which results in a >10,000× gain in sensitivity in the detection of hyperpolarized compounds, means that it is now possible to image the hyperpolarized compound and its metabolic conversion into other metabolites at much higher resolution[35–37]. This technique, which should be applicable clinically, offers many new possibilities for imaging tissue function *in vivo*[36,38].

Voxel volume
The volume of the volume elements of the image. For example, an image with a resolution of 0.1 × 0.1 × 1.0 mm would have a voxel volume of 10 nl.

PET and SPECT. These are radionuclide imaging techniques, which provide relatively low-resolution images of injected probe molecules that have been labelled with positron-emitting (PET) or γ-emitting isotopes (SPECT) (BOX 3). The sensitivity of PET is in the picomolar range, which means that many biological processes can be investigated without any adverse pharmacological effects from the labelled probe molecule[39]. An important advantage of PET over SPECT is that positron-emitting isotopes can usually be substituted for naturally occurring atoms in the probe compound and are therefore less perturbing of probe function. However, the generally long half-lives of SPECT isotopes, or the parent radionuclides from which they are made in radionuclide generators, make them more readily available, whereas the short half-lives of the PET isotopes means that their production and use often requires expensive on-site cyclotron and radiochemistry facilities.

Fluorescence and bioluminescence imaging. In fluorescence imaging, excitation light in the visible region (400–600 nm) is used to excite fluorophores in the tissue, which emit fluorescence at longer wavelengths. Although the technique has been widely used with cultured cells it is limited *in vivo* by the depth of penetration of the excitation light (1–2 mm). This can be increased by using light in the near-infrared (NIR) region of the spectrum (650–900 nm), for which absorption by haemoglobin and water is relatively low[7]. Several NIR fluorochromes have been developed and these have been conjugated to antibodies and peptides for imaging receptor expression[40,41]. These could be used in conjunction with endoscopy to detect early-stage disease in the gastrointestinal tract and in theatre to detect residual disease following surgery[42]. 'Molecular beacons' that are activated by enzyme activity have been developed, for example, peptide-conjugated mutually quenched NIR fluorophores that are activated by matrix metalloproteinase activity and thus can be used to image the activity of the enzyme *in vivo*[43,44]. In fluorescence-mediated tomography, the subject is exposed to continuous-wave or pulsed light sources from different angles and the emitted fluorescence is used to construct a tomographic image. Image resolutions of 1–2 mm have been achieved with a fluorophore detection threshold in the nanomolar range[7]. NIR light has been shown to penetrate at least 10 cm through breast tissue and, in patients with breast tumours, accumulation of indocyanine green in some tumours was detected by its absorption of NIR light. This was correlated with tumour enhancement in DCE-MRI[45].

Recent developments in endoscopy include the incorporation of high-resolution imaging techniques into the endoscope, such as confocal microscopy and optical coherent tomography, which allow a sort of virtual biopsy to be performed[46]. An advantage of these endoscopy measurements is that biopsies can be taken immediately from suspicious lesions and thus the imaging measurement can be validated using the gold standard of histopathology. A problem with these methods is the restricted field of view that can be imaged within a reasonable time frame. However, a new approach, optical frequency-domain imaging, can deliver imaging speeds that are orders of magnitude faster and enables imaging *in vivo* over large tissue areas (>25 cm^2) at depths of up to 2 mm, with a three-dimensional resolution of approximately 15 μm × 15 μm × 10 μm (REF. 47). Although optical coherent tomography and optical frequency-domain imaging cannot be used to detect fluorescence, there are several molecular contrast methods that are compatible with these techniques, such as coherent anti-Stokes Raman spectroscopy and protein-based probes[48]. Raman spectroscopy of biopsy specimens from patients with Barrett oesophagus appeared to provide a sensitive and specific technique for the identification and classification of neoplasia[49] and studies in cultured mammalian cells showed that Raman spectroscopy could detect biochemical changes associated with proliferation[50]. Therefore combination of Raman spectroscopy with endoscopy could provide a label-free method for detecting early stage neoplastic lesions in the gastrointestinal tract.

Bioluminescence imaging relies on the genetic engineering of tissues to express luciferases. These are photoproteins, isolated from organisms such as the firefly, which modify their substrates and in so doing produce light, which can be detected using sensitive cooled charge-coupled device cameras. The advantage over fluorescence imaging is that the technique is very sensitive, as there is no background, with detection

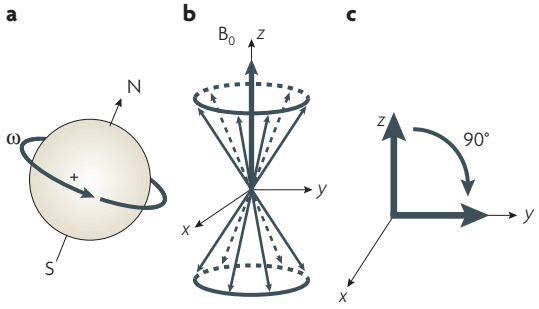

Figure 2 | **Some basic principles of magnetic resonance. a** | Some nuclei have the property of spin and as a consequence possess a magnetic dipole moment. **b** | When placed in a strong magnetic field (B_0) these dipoles tend to align with the field, although not precisely. Instead, they precess around the field at a frequency that is characteristic for a particular nucleus and for the chemical environment of that nucleus. For a spin ½ nucleus, such as the proton, the spins will align with the field (lower energy level) and against the field (higher energy level). There is a slight excess of spins in the lower energy level and thus a net magnetization vector along the *z* axis, or the direction of the applied magnetic field. **c** | Application of an oscillating magnetic field that is perpendicular to the main field (B_0) and rotating at the same frequency as, or resonant with, the nuclear spin precession frequency induces transitions between the two energy levels and tips the net magnetization vector into the *x*–*y* plane. Magnetization in this plane produces a detectable signal in the receiver coil. The second magnetic field is usually applied in the form of a pulse. In the example shown this is a 90° pulse, which it tips the magnetization through 90°. ω, angular velocity.

Cyclotron
A particle accelerator. Collision of a particle (for example, a proton or deuteron) with a target can be used to produce a short-lived positron-emitting isotope.

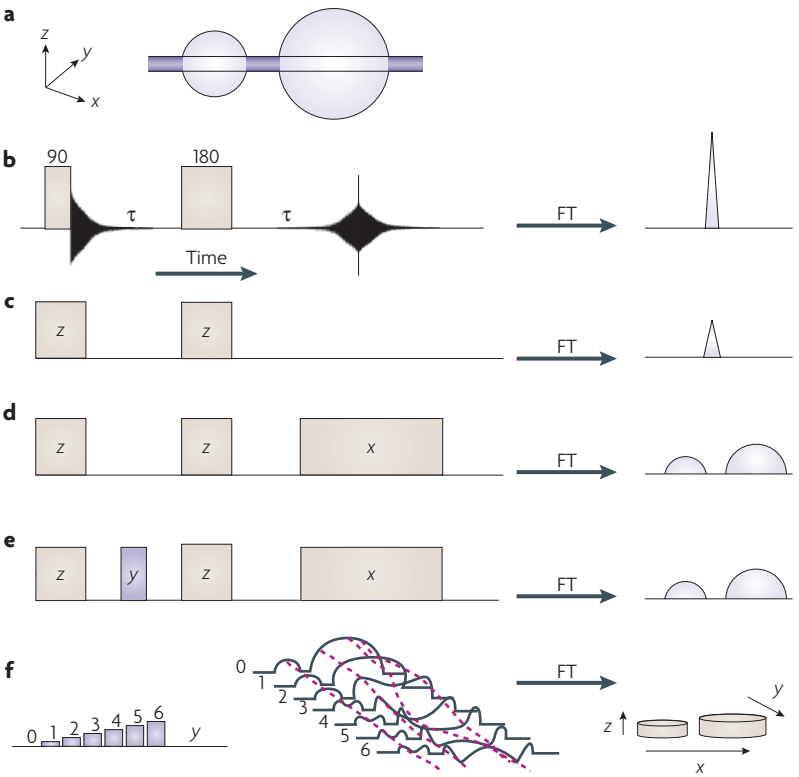

Figure 3 | **The basic principles of an MRI experiment.** The essential principle of magnetic resonance imaging (MRI) is that the resonant frequency of the detected nucleus is a linear function of the applied magnetic field. Thus, if a magnetic field gradient is applied across the sample, the resonant frequency of the nucleus is a function of its spatial position within that gradient. Imagine two spheres containing water (**a**). Application of a 90° pulse tips the water proton magnetization into the *x*–*y* plane, where the observed magnetization decays owing to spin–spin relaxation (T_2) and loss of phase coherence owing to magnetic field inhomogeneity. The loss of phase coherence due to inhomogeneity can be refocused using a 180° pulse, resulting in the formation of a 'spin echo' at time 2τ. Fourier transformation (FT) of the amplitude–time domain signal produces an amplitude (*y* axis)–frequency (*x* axis) spectrum. The water protons in the spheres give rise to a single peak in this spectrum (**b**). If the 90° and 180° pulses are applied in the presence of a linear magnetic field gradient along the *z* axis, and the pulses have limited bandwidth, then they will excite a relatively narrow range of frequencies corresponding to water protons in a *z* slice through the spheres (**c**). The water protons in the spheres still give rise to a single peak, but this is reduced in intensity as it is now only from water protons in the selected *z* slice. If the signal is acquired in the presence of a linear magnetic field gradient along the *x* axis then the resulting spectrum shows a profile of the spheres along this axis (**d**). There are fewer water protons in the smaller sphere and these resonate at higher frequencies because of the *x*-axis field gradient. Application of a phase-encoding gradient along the *y* axis (**e**) during the first time period, τ, causes the phase of the resulting echo to vary as a function of the position of the nuclear spin in the *y* gradient. Acquisition of a series of profiles as a function of an incremented phase-encoding gradient along the *y* axis results in phase modulation of the profiles at a frequency that is dependent on the position of the spins in the *y*-axis gradient. Fourier transformation of this phase modulation produces a profile of the sample in the *y* direction and hence a two-dimensional image of a slice through the sample (**f**). This experiment, which forms the basis of many MRI experiments, illustrates the basic principles of image formation.

sensitivity possibly as low as 10^{-17}–10^{-15} M[51]. However, like fluorescence imaging, scattering and absorption of the emitted photons limits the depth at which the luciferase label can be detected to 1–2 mm. Although the technique has proved useful in the laboratory to monitor gene expression[52], track labelled cells[53], monitor the effects of therapy on established tumours[54] and detect early signs of tumour formation in genetically engineered animals[55], it is unlikely to translate directly to the clinic.

Detecting and predicting response to treatment

The aim is to detect early indications of response, and thus predict the likely outcome of treatment, and also to detect predictive markers of response, which might indicate those patients that are most suitable for a particular therapy. Markers of response include, for example, changes in metabolism or receptor expression associated with tumour cell death or inhibition of proliferation, whereas predictors of response might include the expression of hormone receptors, which predict response to anti-hormonal treatment, or the presence of tumour hypoxia, which can affect the effectiveness of radiotherapy. As well as being used to individualize patient treatment and provide earlier indications of drug efficacy, these techniques might also provide a new approach to drug development. Currently, new treatments are often assessed in patients in end-stage disease, in whom conventional therapies have usually failed. These are arguably the worst patient group in which to try a new drug. However, by using an imaging technique that could give a read-out of drug effectiveness within a few days, as opposed to weeks or months, it might become acceptable to try new treatments in patients who are in the early stages of disease. However, the idea of tailoring therapy to individual patients, by selecting drugs that show early indications of efficacy, remains an aspiration, as at the present time treatment choices are still limited and there is little evidence at the moment that a patient that fails a first-line therapy will respond to a different treatment.

Metabolism

Glycolysis. Tumours have high rates of aerobic glycolysis, as was recognized by Warburg more than 70 years ago, and therefore take up relatively large amounts of the glucose analogue 2-[^{18}F]fluoro-2-deoxy-D-glucose (FDG)[56]. FDG is taken up by glucose transporters and phosphorylated by hexokinase, the first enzyme in the glycolytic pathway. However, the resulting FDG 6-phosphate is not significantly further metabolized and remains trapped in the cell, where the incorporated ^{18}F label can be detected by PET. This is facilitated by the relatively long half-life of ^{18}F (110 min), which is long compared with the time taken for blood clearance of FDG (30–60 min). Studies in animal models of cancer showed that FDG uptake was correlated with the level of expression of the glucose transporter GLUT1 (also known as SLC2A1) and the number of viable cancer cells[57,58]. FDG PET is now well-established clinically in the diagnosis and management of various malignancies and most clinical PET studies use FDG[39,59]. Studies in lung[60], oesophageal[61], lymphoma[62], breast[63] and ovarian cancer[64] have demonstrated that reduced FDG uptake can identify responders early following treatment (FIG. 6). Persistently increased FDG uptake after treatment is associated with a high risk for early disease recurrence and poor prognosis. In gastrointestinal stromal tumours that were treated with the receptor

Box 1 | **Generating contrast in the magnetic resonance image**

Signal intensity in a conventional ^{1}H image of tissue water can be sensitized to various properties of the proton nuclear spin, including the spin relaxation times (T_1 and T_2) and the diffusion constant of the water molecule. As the relaxation times depend on the interaction of the water molecule with other molecules in the tissue, such as proteins, this can give rise to significant contrast in appropriately weighted images. The relaxation times, and thus image contrast, can also be affected by the presence of introduced paramagnetic contrast agents. These can be T_2 agents, such as superparamagnetic iron oxide nanoparticles, which reduce signal intensity in T_2-weighted images, or T_1 agents, such as Gd^{3+} chelates, that increase signal intensity in T_1-weighted images. There are also the so-called paramagnetic chemical exchange saturation transfer (PARACEST) agents, in which the presence of the contrast agent is detected by transfer of magnetization from the small pool of water bound to a lanthanide chelate to the free bulk pool[138]. Destruction of the polarization of the bound water, by selective irradiation, leads to a loss in signal intensity from water in the free bulk pool. To be detectable, the tissue concentration of the lanthanide chelates needs to be in the range of 10^{-5}–10^{-4} M[139]. An interesting variation on this approach is the HYPER-CEST experiment, in which the contrast agent is a cryptophane cage that binds hyperpolarized ^{129}Xe (BOX 2). Selective irradiation of the bound hyperpolarized ^{129}Xe resonance results in loss of its polarization and, through exchange, loss of polarization of the much higher-concentration free ^{129}Xe, leading to a decrease in its signal intensity[140]. With both types of CEST experiment, the small signal from the bound water or ^{129}Xe is effectively amplified by detecting changes in signal intensity of the free species.

tyrosine kinase inhibitor imatinib, response in terms of a marked reduction in FDG uptake was evident as early as 24 h after the first dose, whereas weeks to months were required before reductions in tumour size could be observed from CT measurements[65]. This rapid change in FDG uptake appears to be mediated by translocation of glucose transporters from the plasma membrane to the cytosol and precedes cell death[66]. In cell lines treated with an epidermal growth factor receptor (EGFR) kinase inhibitor, gefitinib, there was a dramatic decrease in FDG uptake as early as 2 h after treatment, which correlated with translocation of the glucose transporter GLUT3 (also known as SLC2A3) from the plasma membrane[67]. This decrease in FDG uptake preceded changes in cell-cycle distribution, thymidine uptake and apoptosis. The translocation of the glucose transporter might be due to inhibition of Akt phosphorylation, which is linked to glucose metabolism in normal and cancer cells.

FDG PET is already being used to individualize therapy. Patients with locally advanced adenocarcinomas of the oesophagogastric junction undergoing neoadjuvant chemotherapy who are classified as non-responders in FDG PET 2 weeks after the start of therapy undergo immediate tumour resection, or chemoradiotherapy when the tumour is not resectable, whereas treatment is continued in the responders[68]. However, FDG PET has a number of limitations. The technique has lower sensitivity for slowly growing, metabolically less-active tumours (such as prostate, thyroid and neuroendocrine tumours) and high levels of uptake in some normal tissues, such as the brain (FIG. 6), can make quantification of tumour uptake difficult. Accumulation in infiltrating inflammatory cells, which also show activation of glycolysis, can limit the sensitivity of the technique for detecting tumour response to treatment[59]. FDG PET data is influenced by various factors, including blood glucose levels, the size of the tumour and data acquisition protocols. Therefore, there have been moves to standardize data acquisition. However, for treatment monitoring it is only necessary to perform a comparison of FDG uptake before and after treatment, and under these circumstances the results are robust to these potentially confounding variables[68].

Treatment-mediated inhibition of tumour glycolysis can also be detected using ^{1}H MRS measurements of lactate concentration, which is produced through the glycolytic pathway. Decreases in tumour lactate concentration in animal tumour models have been reported after chemotherapy or radiation therapy[69]. These measurements have the advantage that they do not require exogenous probe molecules and avoid exposure of the patient to ionizing radiation. However, it remains to be determined whether they have sufficient sensitivity to detect tumour response to therapy in the clinic.

The new technique of spin hyperpolarization (BOX 2), which radically increases sensitivity in the MR experiment, has provided a new way of imaging tumour response to treatment[37,70]. We showed recently that exchange of hyperpolarized ^{13}C label between the carboxyl groups of lactate and pyruvate, in the reaction catalysed by the enzyme lactate dehydrogenase, could be imaged in tumours and that this flux was decreased in treated tumours undergoing drug-induced cell death[71] (FIG. 5). This technique could be used in the future for response monitoring in the clinic.

DNA synthesis. Tumour cell proliferation and response to therapy have been assessed in the clinic from PET measurements of 2[^{11}C]thymidine uptake[72]. Correlations have been demonstrated between the fractional retention of 2[^{11}C]thymidine, obtained from kinetic modelling, and histological measurements of tumour cell proliferation, assessed using Ki67 immunohistochemistry[73]. The main limitation, however, is the short half-life of ^{11}C (20 min), and therefore interest has been growing rapidly in the thymidine analogue 3′-deoxy-3′-[^{18}F]fluorothymidine (FLT; half-life 110 min)[74]. This is phosphorylated to FLT 5-phosphate, and thus trapped in the cell, by cytosolic thymidine kinase 1, which is upregulated during the S phase of the cell cycle. In contrast to thymidine, FLT is not incorporated into DNA; however, clinical studies have demonstrated a correlation with cell proliferation[75] and studies in animals have shown that tumour treatment results in a rapid decrease in FLT uptake, which is correlated with *ex vivo* measurements of cell proliferation. In patients, FLT uptake is generally less than that of FDG, which may make assessment of proliferation difficult; nevertheless recent studies in breast cancer have demonstrated that FLT PET can give an early indication of response to treatment[76]. The potential advantages of FLT over FDG for monitoring of response include lower uptake after an inflammatory response, better imaging of brain tumours and possibly increased sensitivity to cytostatic therapies, which often have a greater effect on cell division than on glucose uptake[39]. For example, in a study on glioma cells *in vitro*, FDG uptake was correlated with the number of viable cells, whereas FLT uptake was correlated with cell proliferation[77].

Spin relaxation times
Loss of net magnetization in the *x*–*y* plane is described by a time constant (T_2) called the spin–spin relaxation time. Return of net magnetization to the *z* axis is described by the spin-lattice relaxation time (T_1). Thus $T_1 \geq T_2$. For water protons in a biological system T_1 is usually of the order of seconds and T_2 tens of milliseconds.

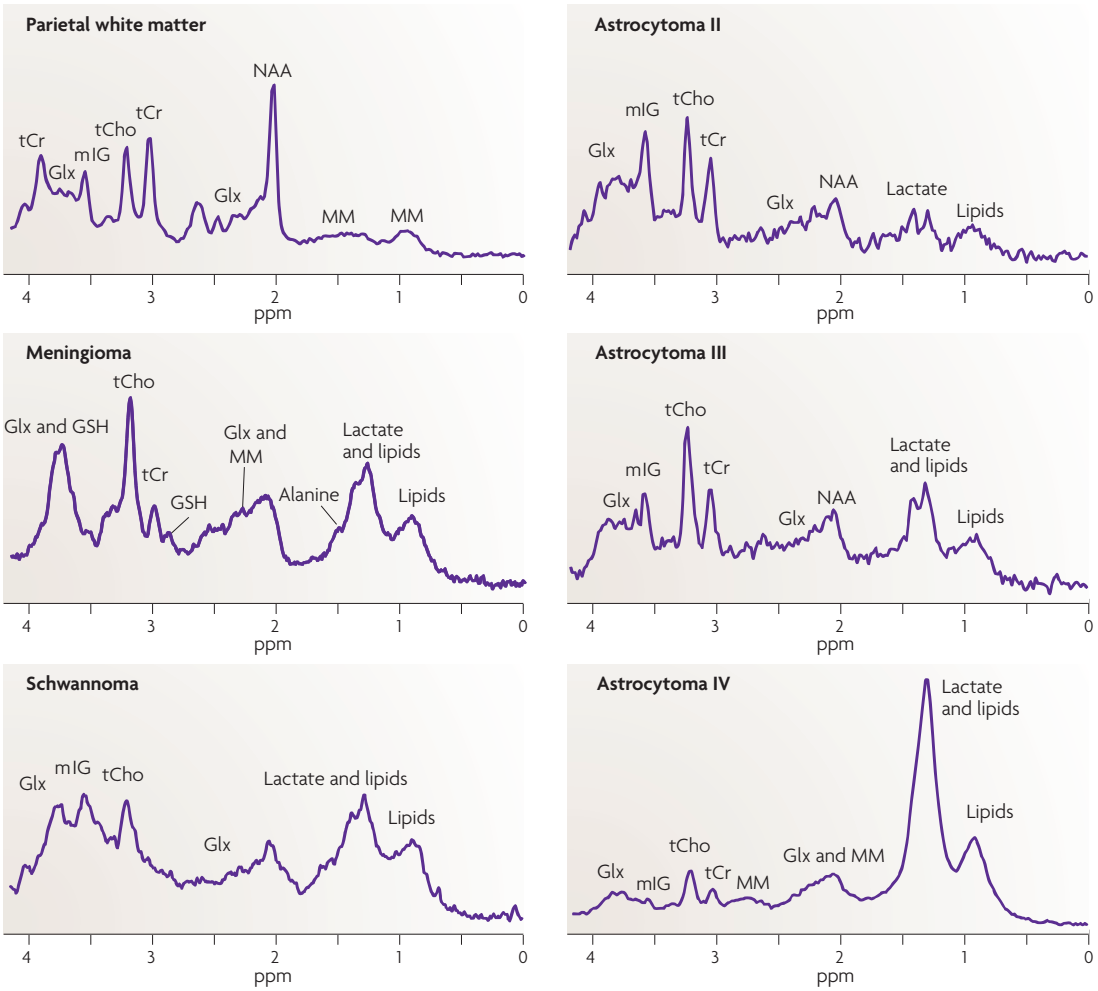

Figure 4 | **Magnetic resonance spectroscopy.** For an NMR-active nucleus the resonance frequency varies (on the order of a few kilohertz, depending on the nucleus) according to its electronic environment. This is known as chemical shift. This figure shows representative ^{1}H spectra from normal human brain and adult brain tumours acquired at 1.5 T using stimulated-echo acquisition mode with an echo time of 30 ms. As the patterns of metabolites are characteristic of the particular tumour type, measurements such as these could eventually be used to diagnose and grade tumours, removing the need for tumour biopsy. Glx; glutamate and glutamine; GSH, glutathione; mIG, *myo*-inositol and glycine; MM, macromolecules; NAA, *N*-acetyl aspartate; tCho, total cholines; tCr, total creatines. Spectra courtesy of F. Howe, St. George's Hospital Medical School, London, UK.

Amino-acid and lipid metabolism. Several amino acids, or amino-acid analogues, have been labelled with positron-emitting isotopes and used for tumour imaging with PET. The principal factor responsible for their increased uptake in tumours seems to be increased expression of the L-type amino acid transporter system[78]. They have been particularly useful in imaging brain tumours, for which imaging with FDG is compromised by the high uptake in normal brain. However, the results of response monitoring, with L-[methyl-^{11}C]methionine, for example, have been mixed. Uptake was reduced in head and neck cancers treated with radiotherapy; however, there was no correlation with treatment outcome[79]. Similarly, in rectal cancer uptake was reduced in tumours undergoing chemoradiotherapy, but this was not correlated with histopathological tumour response[80], and in lung cancer treated with radiotherapy uptake was reduced, but this did not provide any more information than was obtained with FDG[81]. However, in glioma reduction of methionine uptake during temozolomide treatment was shown to predict a favourable clinical outcome[82], and in low-grade astrocytoma patients treated with radiotherapy stable or decreasing methionine uptake following treatment correlated with treatment response[83].

In normal tissues [1-^{11}C]acetate is rapidly oxidized and the label cleared as $^{11}CO_2$. However, in many cancer cells the labelled acetate is used in the synthesis of fatty acids by the enzyme fatty acid synthase, trapping the label in the cells[84]. A key treatment decision in prostate cancer is based on whether the disease is localized in the prostate, and thus amenable to radiotherapy, or widespread, which requires treatment with androgen ablation or chemotherapy. Prostate cancer cells have increased fatty acid synthase levels[85] and

L-type amino-acid transporter system
The L-type amino-acid transporter is a Na^+-independent neutral amino-acid transporter that has a broad substrate selectivity and has been shown to be upregulated in some cancers.

Box 2 | **Nuclear spin hyperpolarization**

Sensitivity in the NMR experiment can be increased dramatically using nuclear spin hyperpolarization techniques. The weak interaction between the nuclear spin and the applied magnetic field means that, for a spin ½ nucleus such as ^{1}H or ^{13}C, the two allowed spin energy levels are nearly equally populated, with a slight excess of spins in the lower energy level. For example, if we had 1×10^{6} proton spins at a field of 2.35 T (100 MHz proton resonance frequency), there would be only 16 extra spins in the lower energy level and thus a very small polarization or net magnetization along the *z* axis (FIG. 2). The conventional way to increase the population difference, and thus the polarization and sensitivity of the NMR experiment, is to use a higher magnetic field. An alternative way is to transfer polarization from an electron or nuclear spin that has a higher polarization. For the noble gases ^{3}He and ^{129}Xe, polarization can be increased dramatically (typically to ~10% for ^{129}Xe and 50% for ^{3}He) by transferring spin polarization, through binary collisions, from rubidium atoms in the vapour phase that have been spin polarized using circularly polarized light from a laser. Hyperpolarized ^{3}He is increasingly being used in the clinic for imaging lung function with ^{3}He magnetic resonance imaging, in which the patient breathes in the hyperpolarized gas[142]. A more versatile technique (dynamic nuclear polarization (FIG. 5)), which in principle can be used with any NMR-active nucleus, involves transferring polarization from a hyperpolarized electron spin. In practice it means using nuclei that, like ^{3}He and ^{129}Xe, have relatively long T_1 relaxation times, for which the lifetime of the polarization is sufficiently long (typically tens of seconds) to be detected in a subsequent imaging experiment.

^{11}C-acetate has been shown to be more sensitive than FDG in detecting recurrent disease[86]. Numerous ^{1}H and ^{31}P MRS studies on isolated tumour cells and tumours *in vivo*, in animal models and in the clinic, have demonstrated altered phospholipid metabolism: there is, in general, an increase in the level of phosphocholine and choline-containing compounds when compared with normal tissues. The level of choline kinase, the first enzyme in the pathway of phosphatidylcholine biosynthesis, has been shown to be increased in biopsy material from animal and human tumours and Ras oncogene transformation can stimulate choline kinase activity, leading to increased levels of phosphocholine[87]. MRS measurements of decreases in the levels of choline-containing compounds following treatment have been shown to be predictive of response in brain, breast and prostate cancer[88,89]. Choline and choline analogues can be labelled with ^{11}C or ^{18}F and used to interrogate phospholipid metabolism using PET. In prostate cancer, for example, there is evidence that the uptake of a choline analogue is decreased early in anti-androgen therapy[90]. The heat-shock protein inhibitor geldanamycin can inhibit the Ras–Raf–mitogen-activated protein kinase kinase (MEK)–extracellular signal-regulated kinase (ERK) signalling pathway and has been shown to result in decreased [methyl-^{14}C]choline uptake, [methyl-^{14}C]phosphocholine production and cell viability[91] in human colon carcinoma cells. A subsequent ^{31}P and ^{1}H MRS study showed an increase in the total concentration of phosphocholine, implying downstream inhibition of the pathway of phosphatidylcholine biosynthesis[92]. On the basis of these studies it was suggested that PET measurements of [methyl-^{11}C]choline uptake, or ^{1}H and ^{31}P MRS measurements of phosphocholine levels, might be useful as pharmacodynamic markers for the evaluation of geldanamycin analogues. However, changes in phospholipid metabolism can also result from the induction of cell death[93] and therefore the changes observed may not be specifically associated with the action of the drug.

Cell death

Increased tumour cell death early during the course of treatment, in preclinical and clinical studies, has been shown to be a good prognostic indicator of outcome[94–97]. MR methods for detecting cell death include ^{1}H MRS measurements of cytoplasmic lipid-droplet accumulation, which accompanies death in some cells, and diffusion-weighted ^{1}H MRI[98]. The latter technique, which has been used clinically, measures the increase in the apparent diffusion coefficient of water, which is thought to be increased in responding tumours owing to a decrease in cellularity[99] (FIG. 7).

A relatively early event in apoptosis is the exposure of phosphatidylserine on the outer leaflet of the plasma membrane bilayer[100]. This can be detected using appropriately labelled agents that bind to this phospholipid using SPECT[101], PET[102], MRI[19,20,103] or optical imaging[104]. Early-stage clinical trials using radiolabelled annexin V (^{99m}Tc-6-hydrazinonicotinic AnxV), however, had limited success owing mainly to poor clearance and biodistribution of the labelled probe[105].

Receptor imaging

The development of drugs that block cell-surface receptors on tumours is a major area of research and probes for imaging receptor expression have been developed for SPECT and PET[106]. For example, patients who show high levels of expression of the somatostatin receptor in thyroid cancer on imaging can be selected for targeted radionuclide therapy with radiolabelled somatostatin analogues[107]. Oestrogen-receptor expression can be imaged with PET using [^{18}F]fluoro-oestradiol, and [^{18}F]fluoro-oestradiol uptake in breast cancer patients was shown to predict response to hormonal treatment[108]. Androgen receptors have been imaged in prostate cancer using 16-[^{18}F]fluoro-5-dihydrotestosterone. Treatment with the androgen antagonist flutamide was shown to decrease 16-[^{18}F]fluoro-5-dihydrotestosterone uptake[109]. The ERBB2 receptor is a member of the EGFR family that is overexpressed in several human tumours, notably in a subset of breast cancers. Recently an ERBB2-specific

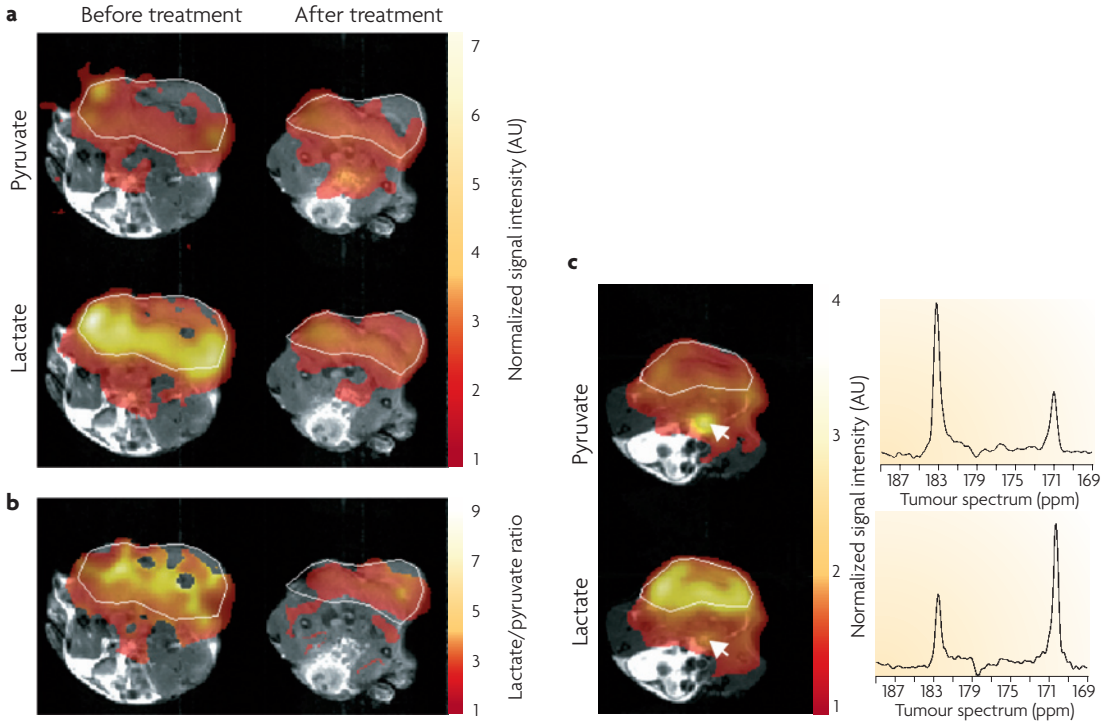

Figure 5 | **^{13}C spectroscopic imaging using hyperpolarized [1-^{13}C]pyruvate.** In a dynamic nuclear polarization experiment a solution of the material to be polarized is mixed with a stable radical and rapidly frozen to form a glass. The electron spin on the radical is polarized (to unity polarization) by cooling the sample to a low temperature (~1.3 K) in a magnetic field. The polarization is then transferred to the nuclear spin by exciting the electron spin resonance. Currently, in favourable cases, nuclear spin polarizations of up to 50% are possible[70]. The polarized compound is then brought rapidly to room temperature, without significant loss of this polarization, and injected into the biological system. As detection of the polarization necessarily involves its destruction, the imaging experiments that are used must make efficient use of this enhanced polarization. The images show ^{13}C spectroscopic imaging of a murine lymphoma following injection of hyperpolarized [1-^{13}C]pyruvate, before and after chemotherapy. Colour maps representing [1-^{13}C]lactate and [1-^{13}C]pyruvate peak intensities (**a**), and plots of corresponding lactate/pyruvate intensity ratios (**b**) obtained from ^{13}C chemical-shift images in the same mouse before and after treatment with etoposide. The images were acquired between 20 and 25 s after hyperpolarized [1-^{13}C]pyruvate injection and 20 h after etoposide treatment. Colour maps representing [1-^{13}C]lactate and [1-^{13}C]pyruvate peak intensities and spectra from the tumour and a blood vessel (indicated by arrow) in an etoposide-treated mouse are shown in (**c**). The ^{1}H images, shown in greyscale, were used to define the tumour margins (indicated by white lines). Data reproduced, with permission, from REF. 71 © (2007) Nature Publishing Group.

radioiodinated affibody was described, which showed good visualization of ERBB2-expressing breast tumour xenografts in mice[110]. Affibodies, which are 6 kDa proteins derived from one of the immunoglobulin G-binding domains of Protein A, show promise as small, high-affinity ligands[110]. Their advantage over antibodies is that, being much smaller, they should penetrate the tumour tissue more readily and also clear more rapidly, thus giving better contrast.

Tumour angiogenesis and vascular function

For a tumour to grow beyond 1–2 mm there is a requirement for the growth of new blood vessels to supply nutrients, in particular, oxygen. This process of angiogenesis is essential for tumour invasion and subsequent metastasis and increased angiogenesis is normally associated with poor prognosis[111]. There has been considerable interest in the development of anti-vascular drugs, which destroy existing tumour vasculature (FIG. 1), and anti-angiogenic drugs, which inhibit blood-vessel growth[112,113]. As these drugs normally arrest tumour growth, rather than produce tumour shrinkage, their action is better imaged using techniques designed to assess vascular function, rather than the more conventional imaging measurements of tumour size[114]. The actions of anti-vascular drugs have been assessed in preclinical and clinical studies using DCE-MRI, in which a series of rapidly acquired images are used to follow the kinetics of contrast agent inflow into the tumour following intravenous injection of the agent[115]. Tumour angiogenesis is associated with an increase in vessel permeability, which can be measured using DCE-MRI techniques[116]. For example, in patients treated with an anti-angiogenic vascular endothelial growth factor receptor tyrosine kinase inhibitor, there were significantly greater reductions in a pharmacokinetic parameter that was related to vessel permeability in patients that showed a positive response to treatment than in those that had progressive disease[117]. Although

Box 3 | **Basic principles of PET and SPECT**

PET

Decay of the positron-emitting isotope results in the collision of the positron with a nearby electron. This results in their mutual annihilation and the emission of two 511 keV γ-ray beams that are orientated at ~180° with respect to one another. The near simultaneous detection of these beams by two scintillation detectors places the isotope on a line between them. By detecting multiple collision events an image of the two-dimensional location of the isotope within the detector ring can be produced (see figure). Subjects are placed within a ring of scintillation detectors and injected with a probe molecule that is labelled with a short half-life positron-emitting isotope, such as ^{15}O ($t_{1/2}$ = 2.03 min), ^{13}N ($t_{1/2}$ = 9.96 min), ^{11}C ($t_{1/2}$ = 20.4 min) or ^{18}F ($t_{1/2}$ = 109.7 min; used as a substitute for ^{1}H), although isotopes with much longer half-lives, for example, ^{64}Cu ($t_{1/2}$ = 12.7 h), are also used. Most clinical positron-emission tomography (PET) scanners have a spatial resolution of 6–8 mm and small-animal scanners now have image resolutions approaching 1 mm.

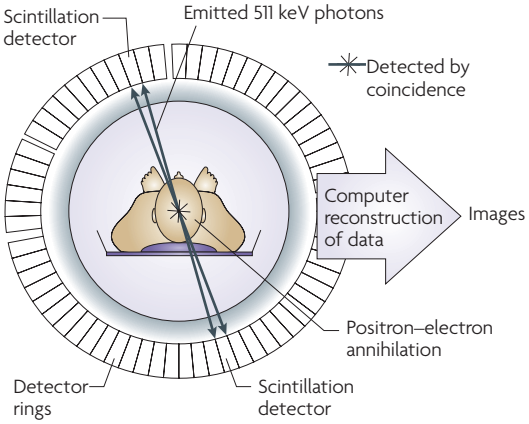

SPECT

The subject is injected with γ-emitting isotopes such as ^{99m}Tc, ^{111}In or ^{123}I, and the γ-rays are detected using γ-cameras that rotate around the subject to produce a tomographic image. Lead collimators, which are used to restrict the detection of the γ-rays to specific, defined directions, markedly reduce the sensitivity of single photon-emission computed tomography (SPECT) when compared with PET, which is at least 10× more sensitive. Decreasing the size of the pinhole in the collimator increases spatial resolution at the expense of sensitivity. This can be offset by using multiple pinholes that, with appropriate image reconstruction algorithms, give image resolutions approaching 0.35 mm in small animals[141].

permeability has been estimated using clinically approved small-molecule contrast agents, this is better done using macromolecular agents and these are currently in clinical development[118]. In animal tumour models, MRI measurements of vascular maturity, assessed from the ability of vessels to dilate in response to breathing CO_2, were shown to predict responsiveness to vascular endothelial growth factor withdrawal, with the immature non-dilating vessels being more sensitive[119]. In another study, pretreatment vascular permeability was correlated with susceptibility to the anti-vascular drug combretastatin A4 3-*O*-phosphate, suggesting that vascular permeability measurements might be used in the clinic to select those patients that would be most responsive to the drug[120]. The integrin $\alpha_v\beta_3$ is upregulated on angiogenic endothelium and radionuclide probes that bind this integrin, and thus can be used to image angiogenesis, have been developed based on cyclic pentapeptides containing the RGD motif[121]. These have the potential to be used in the clinic for assessing the effects of anti-angiogenic drugs.

Related to the abnormal vasculature of tumours is heterogeneous and intermittent blood flow, which results in transient periods of hypoxia. Hypoxia, which is observed in 50–60% of all solid tumours, is associated with tumour progression, increased metastatic potential and resistance to radiotherapy. Consequently, there has been considerable interest in the development of methods for imaging tumour hypoxia[122]. These have focused on the use of 2-nitroimidazoles as the imaging probes, which bind to cellular macromolecules as a result of hypoxia-dependent irreversible bioreduction by cellular nitroreductases in hypoxic regions. As binding requires intact nitroreductase enzymes, the probes detect only viable hypoxic cells and not necrotic cells. Appropriately labelled probes have been developed for PET, MRS and SPECT. One of the most widely used has been [^{18}F]fluoro-misonidazole, and PET imaging of hypoxia has demonstrated potential for monitoring the effect of therapy and predicting response[123,124].

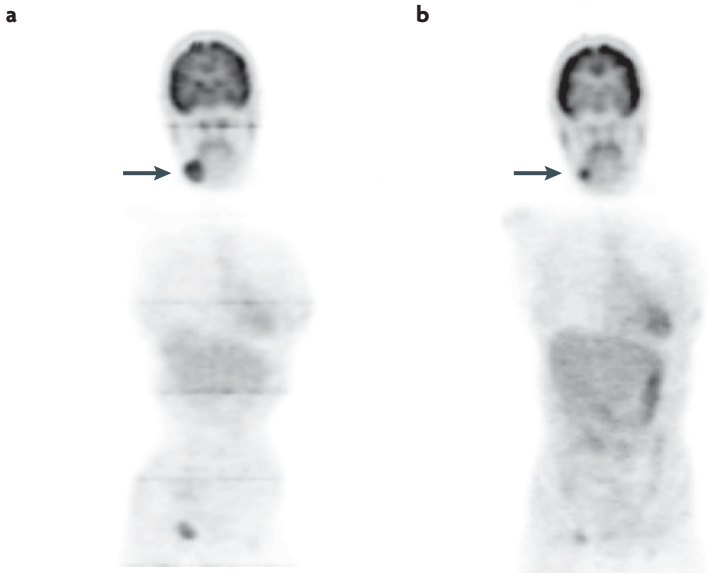

Figure 6 | **Tumour response detected using FDG PET.** A 2-[^{18}F]fluoro-2-deoxy-D-glucose (FDG) positron-emission tomography (PET) image obtained from a patient with lymphoma (arrowed) before (**a**) and after (**b**) drug treatment. Note the high FDG uptake in the tumour and also the brain and the reduction in tumour uptake following drug treatment. Data courtesy of U. Haberkorn, Deutsches Krebsforschungszentrum, Heidelberg, Germany.

Outlook

Current imaging readouts can be relatively non-specific, for example, decreased FDG uptake after therapy could be due to loss of viable cells in the tumour, or downregulation of the glucose transporters or hexokinase activity. However, a thorough knowledge and understanding of the biology of a particular tumour might enable us to ask specific questions using these simple readouts. For example, Akt induces hexokinase expression and Akt-stimulated glycolysis in glioblastoma cells can be inhibited with phosphatidylinositol 3-kinase inhibitors, so it has been suggested that the action of these inhibitors might be imaged using FDG PET. Similarly, fatty acid synthase expression is also regulated by the phosphatidylinositol 3-kinase–Akt pathway and, therefore, [^{11}C]acetate uptake might provide another read-out for the activity of this pathway[125]. In human breast cancer cells expressing a dominant-negative p53 mutant, both hexokinase activity and FDG uptake were increased, suggesting that FDG PET might be used to interrogate drug modulation of p53 activity[126].

The information content could be increased by multimodality imaging, for example, we may be able to distinguish between loss of viable cells and downregulation of glucose transporter or hexokinase activity by using PET-MRI, in which diffusion-weighted MRI is used to assess viable cell density[99]. The differentiation status of hepatocellular carcinomas has been assessed using dual FDG and [^{11}C]acetate PET: the well-differentiated tumours accumulated [^{11}C]acetate whereas the poorly differentiated tumours were FDG-avid[127].

With high-resolution imaging techniques, such as MRI, probe uptake is frequently analysed in manually defined regions of interest, effectively discarding much of the information that may be in the image. This can be considerable, as was demonstrated in a recent study in which CT images were systematically correlated with gene expression profiles of primary human liver cancer. An adapted module networks algorithm was used to search for associations between expression levels of 6,732 genes and combinations of imaging traits. Combinations of 28 imaging traits were shown to reconstruct 78% of the global gene expression profiles. Furthermore, the association map identified novel imaging traits, associated with specific gene-expression signatures that could be used as prognostic indicators of patient survival[128]. The imaging traits were identified manually, but in the future it may be possible to identify these in a fully automated way[129].

Developing imaging techniques that report on some specific biological aspect of a tumour in the clinic will benefit enormously from the development of superior animal models of disease that better reproduce this biology and the response of the tumour to treatment[130]. Thus, we will be able to validate the imaging method in the animal model before transferring to the clinic, possibly in an iterative process. A primary interest in molecular imaging has been targeted imaging probes, for which the use of combinatorial chemistry, phage display and high-throughput screening methods has greatly assisted the development of new probes[131–133]. However, although there have been some significant successes, targeted probes can lack specificity, they can suffer from poor tissue penetration and clearance, which limits contrast development, they often only target cell-surface markers and in general the imaging signal cannot be amplified. There has been considerable interest in gene reporter constructs for use with PET and MRI[134]. Reporters include, for example, herpes simplex virus thymidine kinase (HSV-tk), which can phosphorylate and trap in the cell ^{18}F-labelled nucleoside analogues for PET detection[135], and ferritin, which is paramagnetic when iron-loaded and can be detected by MRI[136]. A primary motivation for developing these has been to provide a means for evaluating the delivery and expression of gene-therapy vectors. In the future, however, when the safety of these vectors has been established, it might be reasonable to consider the development of diagnostic vectors[134]. In these, the expression of the PET- or MRI-detectable reporter could be linked to an intracellular signalling event. For example, PET was used to image transcriptional regulation of p53-dependent genes *in vivo* by constructing a viral vector in which the PET-detectable HSV-tk reporter gene was placed under control of an artificially constructed *cis*-acting p53-specific enhancer. In virally transduced tumour xenografts, DNA damage-induced upregulation of p53 transcriptional activity could be imaged through trapping of an ^{18}F-labelled nucleoside analogue[137]. These vectors, which allow us to readily target intracellular processes, should, in principle, be more specific than the targeted agents in current use, and the imaging signal is amplifiable.

New developments in the field of molecular imaging have mainly been focused in the preclinical arena. In the future, however, we can expect translation of these increasingly sophisticated imaging techniques, which are based on a thorough understanding of the underlying biology and which have been validated in realistic animal models of the disease, to the clinic. Radiologists in the future will need to understand biology as well as anatomy.

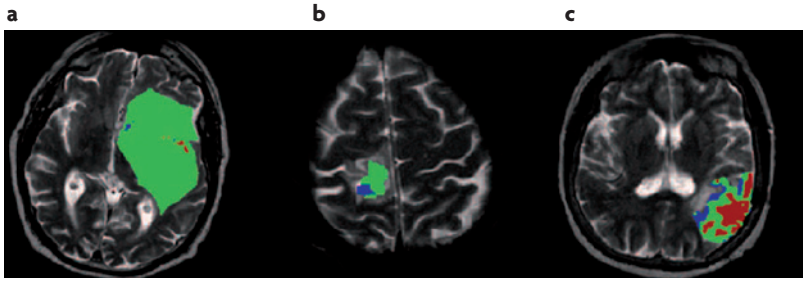

Figure 7 | **Tumour responses detected by diffusion-weighted MRI.** Magnetic resonance images (MRIs) of three patients with oligodendrogliomas. The images were obtained 3 weeks into a 7-week fractionated ionizing radiation treatment. The spatial distribution of changes in the apparent diffusion coefficient of water are shown as colour overlays for patients with progressive disease (**a**), stable disease (**b**) and a patient whose tumour showed a partial response (**c**). The red pixels indicate areas of increased diffusion, blue pixels indicate areas where there was decreased diffusion and green pixels indicate areas where there was no change. There is a general increase in apparent diffusion coefficient in the patient whose tumour subsequently showed a partial response, defined as a 50% decrease in tumour volume observed at least 4 weeks after the conclusion of therapy and on stable or decreased dosage of steroids. Data reproduced, with permission, from REF. 99 © (2005) The National Academy of Sciences.

1. Paez, J. G. *et al. EGFR* mutations in lung cancer: Correlation with clinical response to gefitinib therapy. *Science* **304**, 1497–1500 (2004).
2. Sotiriou, C. & Piccart, M. J. Taking gene-expression profiling to the clinic: when will molecular signatures become relevant to patient care? *Nature Rev. Cancer* **7**, 545–553 (2007).
3. Galbraith, S. M. *et al.* Combretastatin A4 phosphate has tumor antivascular activity in rat and man as demonstrated by dynamic magnetic resonance imaging. *J. Clin. Oncol.* **21**, 2831–2842 (2003).
4. Therasse, P. *et al.* New guidelines to evaluate the response to treatment in solid tumors. European Organization for Research and Treatment of Cancer, National Cancer Institute of the United States, National Cancer Institute of Canada. *J. Natl Cancer Inst.* **92**, 205–216 (2000).
5. Michaelis, L. C. & Ratain, M. J. Measuring response in a post-RECIST world: from black and white to shades of grey. *Nature Rev. Cancer* **6**, 409–414 (2006).
6. Weissleder, R. & Mahmood, U. Molecular imaging. *Radiology* **219**, 316–333 (2001).
A relatively early review from a pioneer (R.W.) of the field of molecular imaging.
7. Weissleder, R. Scaling down imaging: molecular mapping of cancer in mice. *Nature Rev. Cancer* **2**, 1–8 (2001).
8. Boone, J. M., Velazquez, O. & Cherry, S. R. Small-animal X-ray dose from micro-CT. *Mol. Imaging* **3**, 149–158 (2004).
9. von Schulthess, G. K., Steinert, H. C. & Hany, T. F. Integrated PET/CT: Current applications and future directions. *Radiology* **238**, 405–422 (2006).
10. Gee, M. S. *et al.* Doppler ultrasound imaging detects changes in tumor perfusion during antivascular therapy associated with vascular anatomic alterations. *Cancer Res.* **61**, 2974–2982 (2001).
11. Czarnota, G. J. *et al.* Ultrasound imaging of apoptosis: high-resolution non-invasive monitoring of programmed cell death *in vitro*, *in situ* and *in vivo*. *Br. J. Cancer* **81**, 520–527 (1999).
12. Pellot-Barakat, C., Sridhar, M., Lindfors, K. K. & Insana, M. F. Ultrasonic elasticity imaging as a tool for breast cancer diagnosis and research. *Curr. Med. Imaging Rev.* **2**, 157–164 (2006).
13. Sinkus, R. *et al.* High-resolution tensor MR elastography for breast tumour detection. *Phys. Med. Biol.* **45**, 1649–1664 (2000).
14. Kaufmann, B. A. & Lindner, J. R. Molecular imaging with targeted contrast ultrasound. *Curr. Opin. Biotechnol.* **18**, 11–16 (2007).
15. Johnson, G. A., Cofer, G., Gewalt, S. L. & Hedlund, L. W. Morphologic phenotyping with MR microscopy: The visible mouse. *Radiology* **222**, 789–793 (2002).
16. Artemov, D., Mori, N., Ravi, R. & Bhujwalla, Z. M. Magnetic resonance molecular imaging of the HER-2/neu receptor. *Cancer Res.* **63**, 2723–2727 (2003).
17. Sipkins, D. A. *et al.* Detection of tumour angiogenesis *in vivo* by $\alpha_v\beta_3$-targeted magnetic resonance imaging. *Nature Med.* **4**, 623–626 (1998).
A relatively early and much cited example of receptor imaging using MRI. A forerunner of later attempts to image angiogenesis using MRI.
18. Winter, P. M. *et al.* Molecular imaging of angiogenesis in nascent vx-2 rabbit tumors using a novel $\alpha_v\beta_3$-targeted nanoparticle and 1.5 Tesla magnetic resonance imaging. *Cancer Res.* **63**, 5838–5843 (2003).
19. Zhao, M., Beauregard, D. A., Loizou, L., Davletov, B. & Brindle, K. M. Non-invasive detection of apoptosis using magnetic resonance imaging and a targeted contrast agent. *Nature Med.* **7**, 1241–1244 (2001).
20. Schellenberger, E. A. *et al.* Annexin V-CLIO: a nanoparticle for detecting apoptosis by MRI. *Mol. Imaging* **1**, 102–107 (2002).
21. Jung, H. I., Kettunen, M. I., Davletov, B. & Brindle, K. M. Detection of apoptosis using the C2A domain of synaptotagmin, I. *Bioconjug. Chem.* **15**, 983–987 (2004).
22. Bulte, J. W. M. & Kraitchman, D. L. Monitoring cell therapy using iron oxide MR contrast agents. *Curr. Pharm. Biotech.* **5**, 567–584 (2004).
23. Aime, S., Barge, A., Cabella, C., Crich, S. G. & Gianolio, E. Targeting cells with MR imaging probes based on paramagnetic Gd(III) chelates. *Curr. Pharm. Biotech.* **5**, 509–518 (2004).
24. Dodd, S. J. *et al.* Detection of single mammalian cells by high resolution magnetic resonance imaging. *Biophys. J.* **76**, 103–109 (1999).
25. Franklin, R. J. M. *et al.* Magnetic resonance imaging of transplanted oligodendrocyte precursors in the rat brain. *NeuroReport* **10**, 1–5 (1999).
26. Bulte, J. W. M. *et al.* Neurotransplantation of magnetically labeled oligodendrocyte progenitors: Magnetic resonance tracking of cell migration and myelination. *Proc. Natl Acad. Sci. USA* **96**, 15256–15261 (1999).
27. Kircher, M. F. *et al. In vivo* high resolution three-dimensional imaging of antigen-specific cytotoxic T-lymphocyte trafficking to tumors. *Cancer Res.* **63**, 6838–6846 (2003).
28. Hu, D.-E., Kettunen, M. I. & Brindle, K. M. Monitoring T-lymphocyte trafficking in tumors undergoing immune rejection. *Magn. Reson. Med.* **54**, 1473–1479 (2005).
29. de Vries, I. J. M. *et al.* Magnetic resonance tracking of dendritic cells in melanoma patients for monitoring of cellular therapy. *Nature Biotech.* **23**, 1407–1413 (2005).
30. Ahrens, E. T., Flores, R., Xu, H. Y. & Morel, P. A. *In vivo* imaging platform for tracking immunotherapeutic cells. *Nature Biotech.* **23**, 983–987 (2005).
31. Preul, M. C. *et al.* Accurate, non-invasive diagnosis of human brain tumors by using proton magnetic resonance spectroscopy. *Nature Med.* **2**, 232–325 (1996).
An early example of the use of MRS and pattern-recognition techniques to classify brain tumours.
32. Tate, A. R. *et al.* Development of a decision support system for diagnosis and grading of brain tumours using *in vivo* magnetic resonance single voxel spectra. *NMR Biomed.* **19**, 411–434 (2006).
33. Gillies, R. J. & Morse, D. L. *In vivo* magnetic resonance spectroscopy in cancer. *Ann. Rev. Biomed. Bioeng.* **7**, 287–326 (2005).
34. Jeffrey, F. M. H., Rajagopal, A., Malloy, C. R. & Sherry, A. D. ^{13}C NMR: A simple yet comprehensive method for analysis of intermediary metabolism. *Trends Biochem. Sci.* **16**, 5–10 (1991).
A readily accessible review from a group that pioneered ^{13}C NMR and ^{13}C-labeling techniques, particularly with multiply labeled compounds, for interrogating cellular metabolism.
35. Golman, K., Ardenkjær-Larsen, J. H., Petersson, J. S., Månsson, S. & Leunbach, I. Molecular imaging with endogenous substances. *Proc. Natl Acad. Sci. USA* **100**, 10435–10439 (2003).
36. Golman, K., in 't Zandt, R. & Thaning, M. Real-time metabolic imaging. *Proc. Natl Acad. Sci. USA* **103**, 11270–11275 (2006).
37. Golman, K., Zandt, R. I., Lerche, M., Pehrson, R. & Ardenkjaer-Larsen, J. H. Metabolic imaging by hyperpolarized ^{13}C magnetic resonance imaging for *in vivo* tumor diagnosis. *Cancer Res.* **66**, 10855–10860 (2006).
38. Golman, K. & Petersson, J. S. Metabolic imaging and other applications of hyperpolarized ^{13}C. *Acad. Radiol.* **13**, 932–942 (2006).
39. Gambhir, S. S. Molecular imaging of cancer with positron emisson tomography. *Nature Rev. Cancer* **2**, 683–693 (2002).
40. Folli, S. *et al.* Antibody-indocyanin conjugates for immunophotodetection of human squamous cell carcinoma in nude mice. *Cancer Res.* **54**, 2643–2649 (1994).
41. Becker, A. *et al.* Receptor-targeted optical imaging of tumors with near-infrared fluorescent ligands. *Nature Biotech.* **19**, 327–331 (2001).
A good example of using a targeted optical agent for tumour detection.
42. Kelly, K., Alencar, H., Funovics, M., Mahmood, U. & Weissleder, R. Detection of invasive colon cancer using a novel, targeted, library-derived fluorescent peptide. *Cancer Res.* **64**, 6247–6251 (2004).
43. Weissleder, R., Tung, C.-H., Mahmood, U. & Bogdanov, A. *In vivo* imaging of tumors with protease-activated near-infrared fluorescent probes. *Nature Biotech.* **17**, 375–378 (1999).
A classic and much cited example of a molecular beacon for measuring tumour-associated protease activity.
44. Alencar, H. *et al.* Colonic adenocarcinomas: near-infrared microcatheter imaging of smart probes for early detection—study in mice. *Radiology* **244**, 232–238 (2007).
45. Ntziachristos, V., Yodh, A. G., Schnall, M. & Chance, B. Concurrent MRI and diffuse optical tomography of breast after indocyanine green enhancement. *Proc. Natl Acad. Sci. USA* **97**, 2767–2772 (2000).
A paper that describes NIR imaging in the human.
46. Inoue, H., Kudo, S.-e. & Shiokawa, A. Technology Insight: laser scanning confocal microscopy and endocytoscopy for cellular observation of the gastrointestinal tract. *Nature Clin. Prac. Gasteroenterol. Hepatol.* **2**, 31–37 (2005).
47. Yun, S. H. *et al.* Comprehensive volumetric optical microscopy *in vivo*. *Nature Med.* **12**, 1429–1433 (2006).
48. Boppart, S. A., Oldenburg, A. L., Xu, C. Y. & Marks, D. L. Optical probes and techniques for molecular contrast enhancement in coherence imaging. *J. Biomed. Optics* **10**, 041208 (2005).
49. Kendall, C. *et al.* Raman spectroscopy, a potential tool for the objective identification and classification of neoplasia in Barrett's oesophagus. *J. Pathol.* **200**, 602–609 (2003).
50. Short, K. W., Carpenter, S., Freyer, J. P. & Mourant, J. R. Raman spectroscopy detects biochemical changes due to proliferation in mammalian cell cultures. *Biophys. J.* **88**, 4274–4288 (2005).
51. Massoud, T. F. & Gambhir, S. S. Molecular imaging in living subjects: seeing fundamental biological processes in a new light. *Genes Dev.* **17**, 545–580 (2003).
An encyclopaedic review from another pioneer (S.S.G.) in the field of molecular imaging.
52. Bhaumik, S. & Gambhir, S. S. Optical imaging of Renilla luciferase reporter gene expression in living mice. *Proc. Natl Acad. Sci. USA* **99**, 377–382 (2002).
53. Hardy, J. *et al.* Bioluminescence imaging of lymphocyte trafficking *in vivo*. *Exp. Hematol.* **29**, 1353–1360 (2001).
54. Sweeney, T. J. *et al.* Visualizing the kinetics of tumor-cell clearance in living animals. *Proc. Natl Acad. Sci. USA* **96**, 12044–12049 (1999).
55. Vooijs, M., Jonkers, J., Lyons, S. & Berns, A. Noninvasive imaging of spontaneous retinoblastoma pathway-dependent tumors in mice. *Cancer Res.* **62**, 1862–1867 (2002).
An elegant example of how to detect early-stage tumours in a mouse model using bioluminescent imaging.
56. Gatenby, R. A. & Gillies, R. J. Why do cancers have high aerobic glycolysis? *Nature Rev. Cancer* **4**, 891–899 (2004).
57. Brown, R., Leung, J. & Fisher, S. Intratumoral distribution of tritiated fluorodeoxyglucose in breast carcinoma: correlation between Glut-1 expression and FDG uptake. *J. Nucl. Med.* **37**, 1042–1047 (1996).
58. Smith, T. A. D. The rate-limiting step for tumor [^{18}F]fluoro-2-deoxy-D-glucose (FDG) incorporation. *Nucl. Med. Biol.* **28**, 1–4 (2001).
59. Juweid, M. E. & Cheson, B. D. Positron-emission tomography and assessment of cancer therapy. *N. Engl. J. Med.* **354**, 496–507 (2006).
60. Weber, W.A *et al.* Positron emission tomography in non-small-cell lung cancer: Prediction of response to chemotherapy by quantitative assessment of glucose use. *J. Clin. Oncol.* **21**, 2651–2657 (2003).
61. Weber, W. A. *et al.* Prediction of response to preoperative chemotherapy in adenocarcinomas of the esophagogastric junction by metabolic imaging. *J. Clin. Oncol.* **19**, 3058–3065 (2001).
62. Spaepen, K. *et al.* Prognostic value of positron emission tomography (PET) with fluorine-18 fluorodeoxyglucose ([^{18}F]FDG) after first-line chemotherapy in non-Hodgkin's lymphoma: is [^{18}F]FDG PET a valid alternative to conventional diagnostic methods? *J. Clin. Oncol.* **19**, 414–419 (2001).
63. Schelling, M. *et al.* Positron emission tomography using [^{18}F]fluorodeoxyglucose for monitoring primary chemotherapy in breast cancer. *J. Clin. Oncol.* **18**, 1689–1695 (2000).
64. Avril, N. *et al.* Prediction of response to neoadjuvant chemotherapy by sequential F-18-fluorodeoxyglucose positron emission tomography in patients with advanced-stage ovarian cancer. *J. Clin. Oncol.* **23**, 7445–7453 (2005).
65. Stroobants, S. *et al.* ^{18}FDG-Positron emission tomography for the early prediction of response in advanced soft tissue sarcoma treated with imatinib mesylate (Glivec). *Eur. J. Cancer* **39**, 2012–2020 (2003).
A well-known example of how FDG PET can detect response before changes in tumour size.
66. Cullinane, C. *et al.* An *in vivo* tumor model exploiting metabolic response as a biomarker for targeted drug development. *Cancer Res.* **65**, 9633–9636 (2005).
67. Su, H. *et al.* Monitoring tumor glucose utilization by positron emission tomography for the prediction of treatment response to epidermal growth factor receptor kinase inhibitors. *Clin. Cancer Res.* **12**, 5659–5667 (2006).

68. Weber, W. A. Positron emission tomography as an imaging biomarker. *J. Clin. Oncol.* **24**, 3282–3292 (2006).
A recent and well-written review of the role of PET in oncology.
69. Poptani, H. *et al.* Detecting early response to cyclophosphamide treatment of RIF-1 tumors using selective multiple quantum spectroscopy (SelMQC) and dynamic contrast enhanced imaging. *NMR Biomed.* **16**, 102–111 (2003).
70. Ardenkjaer-Larsen, J. H. *et al.* Increase in signal-to-noise ratio of >10,000 times in liquid-state NMR. *Proc. Natl Acad. Sci. USA* **100**, 10158–10163 (2003).
The first description of dissolution dynamic nuclear polarization, a technique that could have an enormous effect on imaging tissue function using magnetic resonance.
71. Day, S. E. *et al.* Detecting tumor response to treatment using hyperpolarized ^{13}C magnetic resonance imaging and spectroscopy. *Nature Med.* **13**, 1382–1387 (2007).
The first example of the use of hyperpolarized magnetic resonance spectroscopic imaging to detect the response of tumours to therapy.
72. Shields, A. F. *et al.* Carbon-11-thymidine and FDG to measure therapy response. *J. Nucl. Med.* **39**, 1757–1762 (1998).
73. Wells, P. *et al.* Assessment of proliferation *in vivo* using 2-[^{11}C]thymidine positron emission tomography in advanced intra-abdominal malignancies. *Cancer Res.* **62**, 5698–5702 (2002).
74. Shields, A. F. *et al.* Imaging proliferation *in vivo* with [^{18}F]FLT and positron emission tomography. *Nature Med.* **11**, 1334–1336 (1998).
The first description of FLT as a PET probe of cell proliferation.
75. Vesselle, H. *et al. In vivo* validation of 3′-deoxy-3′-[^{18}F]fluorothymidine ([^{18}F]FLT) as a proliferation imaging tracer in humans: correlation of [^{18}F]FLT uptake by positron emission tomography with Ki-67 immunohistochemistry and flow cytometry in human lung tumors. *Clin. Cancer Res.* **8**, 3315–3323 (2002).
76. Pio, B. S. *et al.* Usefulness of 3′-[^{18}F]fluoro-3′-deoxythymidine with positron emission tomography in predicting breast cancer response to therapy. *Mol. Imaging Biol.* **8**, 36–42 (2006).
77. an Waarde, A., Been, L. B., Ishiwata, K., Dierckx, R. A. & Elsinga, P. H. Early response of sigma-receptor ligands and metabolic PET tracers to 3 forms of chemotherapy: an *in vitro* study in glioma cells. *J. Nucl. Med.* **47**, 1538–1545 (2006).
78. Jager, P. L. *et al.* Radiolabeled amino acids: basic aspects and clinical applications in oncology. *J. Nucl. Med.* **42**, 432–445 (2001).
79. Nuutinen, J., Jyrkkiö, S., Lehikoinen, P., Lindholm, P. & Minn, H. Evaluation of early response to radiotherapy in head and neck cancer measured with [^{11}C]methionine-positron emission tomography. *Radiother. Oncol.* **52**, 225–232 (1999).
80. Wieder, H. *et al.* PET imaging with [^{11}C]methyl-L-methionine for therapy monitoring in patients with rectal cancer. *Eur. J. Nuc. Med. Mol. Imaging* **29**, 789–796 (2002).
81. Ishimori, T. *et al.* ^{18}F-FDG and ^{11}C-methionine PET for evaluation of treatment response of lung cancer after stereotactic radiotherapy. *Ann. Nucl. Med.* **18**, 669–674 (2004).
82. Galldiks, N. *et al.* Use of ^{11}C-methionine PET to monitor the effects of temozolomide chemotherapy in malignant gliomas. *Eur. J. Nuc. Med. Mol. Imaging* **33**, 516–524 (2006).
83. Nuutinen, J. *et al.* Radiotherapy treatment planning and long-term follow-up with [^{11}C]methionine pet in patients with low-grade astrocytoma. *Int. J. Radiat. Oncol. Biol. Phys.* **48**, 43–52 (2000).
84. Yoshimoto, M. *et al.* Characterization of acetate metabolism in tumor cells in relation to cell proliferation: Acetate metabolism in tumor cells. *Nucl. Med. Biol.* **28**, 117–122 (2001).
85. Jana, S. & Blaufox, M. D. Nuclear medicine studies of the prostate, testes, and bladder. *Semin. Nucl. Med.* **36**, 51–72 (2006).
86. Oyama, N. *et al.* ^{11}C-acetate PET imaging of prostate cancer: detection of recurrent disease at PSA relapse. *J. Nucl. Med.* **44**, 549–555 (2003).
87. Glunde, K., Jacobs, M. A. & Bhujwalla, Z. M. Choline metabolism in cancer: implications for diagnosis and therapy. *Expert Rev. Mol. Diag.* **6**, 821–829 (2006).
A recent review of the role of choline metabolism in tumour cell proliferation and different ways of imaging this from a group that has been very active in this field.
88. Meisamy, S. *et al.* Neoadjuvant chemotherapy of locally advanced breast cancer: predicting response with *in vivo* ^{1}H MR spectroscopy — A pilot study. *Radiology* **233**, 424–431 (2004).
89. Kurhanewicz, J., Vigneron, D. B. & Nelson, S. J. Three-dimensional magnetic resonance spectroscopic imaging of brain and prostate cancer. *Neoplasia* **2**, 166–189 (2000).
90. DeGrado, T. R. *et al.* Synthesis and evaluation of ^{18}F-labeled choline as an oncologic tracer for positron emission tomography: Initial findings in prostate cancer. *Cancer Res.* **61**, 110–117 (2001).
91. Liu, D. *et al.* Use of radiolabelled choline as a pharmacodynamic marker for the signal transduction inhibitor geldanamycin. *Br. J. Cancer* **87**, 783–789 (2002).
92. Chung, Y. L. *et al.* Magnetic resonance spectroscopic pharmacodynamic markers of the heat shock protein 90 inhibitor 17-allylamino, 17-demethoxygeldanamycin (17AAG) in human colon cancer models. *J. Natl Cancer Inst.* **95**, 1624–1633 (2003).
MRS as a tool for detecting drug action.
93. Anthony, M. L., Zhao, M. & Brindle, K. M. Inhibition of phosphatidylcholine biosynthesis following induction of apoptosis in HL-60 cells. *J. Biol. Chem.* **274**, 19686–19692 (1999).
94. Dubray, B. *et al. In vitro* radiation-induced apoptosis and early response to low-dose radiotherapy in non-Hodgkin's lymphomas. *Radiother. Oncol.* **46**, 185–191 (1998).
95. Chang, J. *et al.* Apoptosis and proliferation as predictors of chemotherapy response in patients with breast carcinoma. *Cancer* **89**, 2145–2152 (2000).
96. Ellis, P. A. *et al.* Preoperative chemotherapy induces apoptosis in early breast cancer. *Lancet* **349**, 849 (1997).
97. Meyn, R. E. *et al.* Heterogeneity in apoptosis development in irradiated murine tumours of different histologies. *Int. J. Radiat. Biol.* **64**, 583–591 (1993).
98. Kettunen, M. I. & Brindle, K. M. Apoptosis detection using magnetic resonance imaging and spectroscopy. *Prog. Nucl. Mag. Reson. Spectrosc.* **47**, 175–185. (2005).
99. Moffat, B. A. *et al.* Functional diffusion map: A noninvasive MRI biomarker for early stratification of clinical brain tumor response. *Proc. Natl Acad. Sci. USA* **102**, 5524–5529 (2005).
A clinically applicable and label-free MRI method for detecting early tumour responses to treatment.
100. Corsten, M. F., Hofstra, L., Narula, J. & Reutelingsperger, C. P. Counting heads in the war against cancer: defining the role of annexin A5 imaging in cancer treatment and surveillance. *Cancer Res.* **66**, 1255–1260 (2006).
A recent review describing the use of labelled annexin to detect cell death.
101. Belhocine, T. *et al.* Increased uptake of the apoptosis-imaging agent ^{99m}Tc recombinant human Annexin V in human tumors after one course of chemotherapy as a predictor of tumor response and patient prognosis. *Clin. Cancer Res.* **8**, 2766–2774 (2002).
102. Cauchon, N. *et al.* PET imaging of apoptosis with ^{64}Cu-labeled streptavidin following pretargeting of phosphatidylserine with biotinylated annexin-V. *Eur. J. Nucl. Med. Mol. Imaging* **34**, 247–258 (2007).
103. Neves, A. A. *et al.* A paramagnetic nanoprobe to detect tumor cell death using magnetic resonance imaging. *Nano Lett.* **7**, 1419–1423 (2007).
104. Petrovsky, A., Schellenberger, E., Josephson, L., Weissleder, R. & Bogdanov, A. Near-infrared fluorescent imaging of tumor apoptosis. *Cancer Res.* **63**, 1936–1942 (2003).
105. Boersma, H. H. *et al.* Past, present, and future of annexin A5: from protein discovery to clinical applications. *J. Nucl. Med.* **46**, 2035–2050 (2005).
106. Van Den Bossche, B. & de Wiele, C. V. Receptor imaging in oncology by means of nuclear medicine: Current status. *J. Clin. Oncol.* **22**, 3593–3607 (2004).
107. Teunissen, J. J. M., Kwekkeboom, D. J. & Krenning, E. P. Staging and treatment of differentiated thyroid carcinoma with radiolabeled somatostatin analogs. *Trends Endocrinol. Metab.* **17**, 19–25 (2006).
108. Linden, H. M. *et al.* Quantitative fluoroestradiol positron emission tomography imaging predicts response to endocrine treatment in breast cancer. *J. Clin. Oncol.* **24**, 2793–2799 (2006).
109. Dehdashti, F. *et al.* Positron tomographic assessment of androgen receptors in prostatic carcinoma. *Eur. J. Nuc. Med. Mol. Imaging* **32**, 344–350 (2005).
110. Orlova, A. *et al.* Tumor imaging using a picomolar affinity HER2 binding affibody molecule. *Cancer Res.* **66**, 4339–4348 (2006).
111. Carmeliet, P. & Jain, R. K. Angiogenesis in cancer and other diseases. *Nature* **407**, 249–257 (2000).
112. Tozer, G. M., Kanthou, C. & Baguley, B. C. Disrupting tumour blood vessels. *Nature Rev. Cancer* **5**, 423–435 (2005).
113. Folkman, J. Angiogenesis. *Annu. Rev. Med.* **57**, 1–18 (2006).
114. Miller, J. C., Pien, H. H., Sahani, D., Sorensen, A. G. & Thrall, J. H. Imaging angiogenesis: Applications and potential for drug development. *J. Natl Cancer Inst.* **97**, 172–187 (2005).
115. Leach, M. O. *et al.* The assessment of antiangiogenic and antivascular therapies in early-stage clinical trials using magnetic resonance imaging: issues and recommendations. *Br. J. Cancer* **92**, 1599–1610 (2005).
A discussion of the methods for assessing response to anti-angiogenic and anti-vascular treatments using dynamic contrast agent-enhanced MRI.
116. McDonald, D. M. & Choyke, P. L. Imaging of angiogenesis: from microscope to clinic. *Nature Med.* **9**, 713–725 (2003).
117. Morgan, B. *et al.* Dynamic contrast-enhanced magnetic resonance imaging as a biomarker for the pharmacological response of PTK787/ZK 222584, an inhibitor of the vascular endothelial growth factor receptor tyrosine kinases, in patients with advanced colorectal cancer and liver metastases: Results from two phase I studies. *J. Clin. Oncol.* **21**, 3955–3964 (2003).
118. Barrett, T., Kobayashi, H., Brechbiel, M. & Choyke, P. L. Macromolecular MRI contrast agents for imaging tumor angiogenesis. *Eur. J. Radiol.* **60**, 353–366 (2006).
119. Abramovitch, R., Dafni, H., Smouha, E., Benjamin, L. E. & Neeman, M. *In vivo* prediction of vascular susceptibility to vascular endothelial growth factor withdrawal: magnetic resonance imaging of C6 rat glioma in nude mice. *Cancer Res.* **59**, 5012–5016 (1999).
120. Beauregard, D. A., Hill, S. A., Chaplin, D. J. & Brindle, K. M. The susceptibility of tumors to the anti-vascular drug combretastatin A4 phosphate correlates with vascular permeability. *Cancer Res.* **61**, 6811–6815 (2001).
121. Haubner, R. *et al.* Noninvasive visualization of the activated $\alpha_v\beta3$ integrin in cancer patients by positron emission tomography and [^{18}F]galacto-RGD. *PLOS Med.* **2**, 244–252 (2005).
122. Ljungkvist, A. S. E., Bussink, J., Kaanders, J. H. A. M. & Van der Kogel, A. J. Dynamics of tumor hypoxia measured with bioreductive hypoxic cell markers. *Radiat. Res.* **167**, 127–145 (2007).
123. Eschmann, S. M. *et al.* Prognostic impact of hypoxia imaging with ^{18}F-misonidazole PET in non-small cell lung cancer and head and neck cancer before radiotherapy. *J. Nucl. Med.* **46**, 253–260 (2005).
124. Gagel, B. *et al.* [^{18}F] fluoromisonidazole and [^{18}F] fluorodeoxyglucose positron emission tomography in response evaluation after chemo-/radiotherapy of non-small-cell lung cancer: a feasibility study. *BMC Cancer* **6**, 51 (2006).
125. Czernin, J., Weber, W. A. & Herschman, H. R. Molecular imaging in the development of cancer therapeutics. *Annu. Rev. Med.* **57**, 99–118 (2006).
126. Smith, T. A. D., Sharma, R. I., Thompson, A. M. & Paulin, F. E. M. Tumor ^{18}F-FDG incorporation is enhanced by attenuation of p53 function in breast cancer cells *in vitro*. *J. Nucl. Med.* **47**, 1525–1530 (2006).
127. Ho, C.-l., Chen, S., Yeung, D. W. C. & Cheng, T. K. C. Dual-tracer PET/CT imaging in evaluation of metastatic hepatocellular carcinoma. *J. Nucl. Med.* **48**, 902–909 (2007).
128. Segal, E. *et al.* Decoding global gene expression programs in liver cancer by noninvasive imaging. *Nature Biotech.* **25**, 675–680 (2007).
A fascinating study correlating defined imaging traits in CT scans with gene-expression profiles,

raising the possibility that gene-expression programmes might be inferred from imaging studies.
129. Zhang, Y. Y., Brady, M. & Smith, S. Segmentation of brain MR images through a hidden Markov random field model and the expectation-maximization algorithm. *IEEE Trans. Med. Imaging* **20**, 45–57 (2001).
130. Frese, K. K. & Tuveson, D. A. Maximizing mouse cancer models. *Nature Rev. Cancer* **7**, 654–658 (2007).
Realistic animal models of disease should assist the development of novel clinical imaging methods. This review describes the current state-of-the-art for these models.
131. Trepel, M., Arap, W. & Pasqualini, R. *In vivo* phage display and vascular heterogeneity: implications for targeted medicine. *Curr. Opin. Chem. Biol.* **6**, 399–404 (2002).
132. Haubner, R. & Wester, H. R. Radiolabeled tracers for imaging of tumor angiogenesis and evaluation of anti-angiogenic therapies. *Curr. Pharm. Design* **10**, 1439–1455 (2004).
133. Aina, O. H. *et al.* From combinatorial chemistry to cancer-targeting peptides. *Mol. Pharm.* **4**, 631–651 (2007).
134. Serganova, I. & Blasberg, R. Reporter gene imaging: potential impact on therapy. *Nucl. Med. Biol.* **32**, 763–780 (2005).
135. Tjuvajev, J. G. *et al.* Imaging adenoviral-mediated Herpes virus thymidine kinase gene transfer and expression *in vivo*. *Cancer Res.* **59**, 5186–5193 (1999).
An early example of a radionuclide-based gene reporter.
136. Genove, G., DeMarco, U., Xu, H. Y., Goins, W. F. & Ahrens, E. T. A new transgene reporter for *in vivo* magnetic resonance imaging. *Nature Med.* **11**, 450–454 (2005).
137. Doubrovin, M. *et al.* Imaging transcriptional regulation of p53-dependent genes with positron emission tomography *in vivo*. *Proc. Natl Acad. Sci. USA* **98**, 9300–9305 (2001).
An early example of the way a PET-based gene reporter can be used to image specific aspects of cell biology *in vivo*.
138. Zhou, J. Y. & van Zijl, P. C. M. Chemical exchange saturation transfer imaging and spectroscopy. *Prog. Nucl. Mag. Res. Sp.* **48**, 109–136 (2006).
139. Aime, S. *et al.* Insights into the use of paramagnetic Gd(III) complexes in MR-molecular imaging investigations. *J. Mag. Res. Imaging* **16**, 394–406 (2002).
140. Schröder, L., Lowery, T. J., Hilty, C., Wemmer, D. E. & Pines, A. Molecular imaging using a targeted magnetic resonance hyperpolarized biosensor. *Science* **314**, 446–449 (2006).
141. Beekman, F. & van der Have, F. The pinhole: gateway to ultra-high-resolution three-dimensional radionuclide imaging. *Eur. J. Nuc. Med. Mol. Imaging* **34**, 151–161 (2007).
142. Salerno, M. *et al.* Hyperpolarized noble gas MR imaging of the lung: Potential clinical applications. *Eur. J. Radiol.* **40**, 33–44 (2001).

Competing interests statement
The author declares competing financial interests: see web version for details.

DATABASES

Entrez Gene:
http://www.ncbi.nlm.nih.gov/entrez/query.fcgi?db=gene
ERBB2 | p53 | SLC2A1 | SLC2A3 | thymidine kinase 1
National Cancer Institute Drug Dictionary:
http://www.cancer.gov/drugdictionary/
combretastatin A4 | etoposide | gefitinib | imatinib | temozolomide

FURTHER INFORMATION

Kevin Brindle's homepage:
http://www.bioc.cam.ac.uk/uto/brindle.html

ALL LINKS ARE ACTIVE IN THE ONLINE PDF